



Electrodeposition of Ni, Sn and Ni–Sn Alloy Coatings from Pyrophosphate-Glycine Bath

U. Lačnjevac, B. M. Jović, and V. D. Jović^z

Institute for Multidisciplinary Research, University of Belgrade, Belgrade 11030, Serbia

In this work the electrodeposition of Ni, Sn and Ni–Sn alloy from the solution containing pyrophosphate and/or glycine has been investigated by cyclic voltammetry (CV), potentiostatic pulse and polarization curve measurements on two substrates, Ni and GC. It has been shown that the process of Sn electrodeposition in pure pyrophosphate solution commences at the potential of about -0.90 V on both substrates being characterized by the formation of isolated 3D crystals and their further growth by the reduction of $[\text{Sn}(\text{Pyr})_2]^{6-}$ complex. On the GC surface Sn 3D crystals remain isolated, following 3D nucleation and growth mechanism which does not fit any of the theoretically predicted models. Ni–Sn alloy deposition in the solution containing both cations (Sn^{2+} , Ni^{2+}) and both anions (pyrophosphate and glycine) occurs by the same growth mechanism as pure Sn deposition by simultaneous reduction of $[\text{Sn}(\text{Pyr})_2]^{6-}$, $[\text{Ni}(\text{Pyr})_2]^{6-}$ and/or $[\text{Ni}(\text{Pyr})_3]^-$ complexes at pH 8.0. Depending on the current density/potential of the Ni–Sn alloy coating deposition onto Ni electrode the composition of the flat and compact coatings varies in the range from 66 to 50 atom% Ni, i.e. 34 to 50 atom% Sn.

© 2012 The Electrochemical Society. [DOI: 10.1149/2.042205JES] All rights reserved.

Manuscript submitted December 19, 2011; revised manuscript received February 3, 2012. Published March 7, 2012.

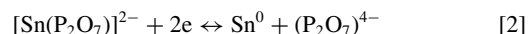
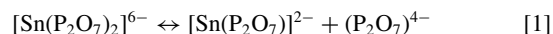
The application field for electrodeposited Ni–Sn alloys is wide. Due to their bright appearance and corrosion resistance they are of great interest for the metal finishing industry.^{1,2} The electronic industry also used electrodeposited Ni–Sn alloys for printed circuit boards as protective and etch-resistant coatings.³ As highly resistant to tarnish and due to their high value of hardness (6–7 GPa) they became an alternative for electroplated chromium in hardware, automotive, electrical and electronics accessories.⁴ Effects of electrodeposition parameters and the bath composition (chloride-fluoride or pyrophosphate bath) on the adhesion, hardness and wear resistance were investigated in the work of Jimenez et al.,⁵ showing that the coatings deposited from chloride-fluoride bath have an overall better performance than those deposited from pyrophosphate bath. Electrodeposited Ni–Sn alloy films have also found application in fabrication of anode for Li-ion batteries.^{6–10}

Concerning phase composition of electrodeposited Ni–Sn alloys in most of the papers it was stated that Ni–Sn alloys exists as single-phase homogeneous intermetallic compound of equiatomic composition NiSn (35 wt % Ni – 65 wt % Sn, 50 atom% Ni – 50 atom% Sn).^{11,12}

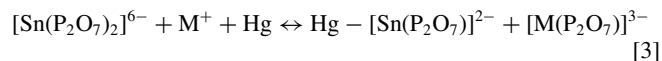
One of the most interesting properties of electrodeposited Ni–Sn alloys is their catalytic activity for hydrogen evolution in alkaline solutions.^{13,14} Detailed investigation of the electrodeposition conditions and their influence on the overvoltage for hydrogen evolution in alkaline solution has been performed in the work of Yamashita et al.¹⁴ By changing the deposition current density and concentration of SnCl_2 in the pyrophosphate–glycine bath, Ni content in the alloy coatings was changed from 20 to 98 wt%, while the overvoltage for hydrogen evolution was found to be practically independent of the alloy composition in the range 40–80 wt% of Ni. The morphology of the coatings was found to change from relatively smooth, fine grain structure, at low plating current density, to nodular one appearing as large spherical particles with the diameter of about 15 μm at high plating current density.¹⁴ By the XRD analysis it was shown that the deposits prepared from the pyrophosphate–glycine bath were composed of only NiSn phase, irrespective of the plating current density, with the x-ray peaks becoming broader in the samples deposited at higher plating current densities. On the basis of these facts, the authors concluded that the catalytic ability is closely related to the line broadening of X-ray diffraction peaks and to the surface state.¹⁴ Although the electrodeposition process was investigated at different current densities and different SnCl_2 concentrations, no explanation of the Ni–Sn alloy electrodeposition mechanism has been given in the above mentioned references.^{11–14}

Electroplating of tin has been known for a long time. Two main types of solutions for tin electroplating, alkali Sn–IV based solutions and acidic Sn–II salt based solutions were used.^{15–19} Electroplating of tin from acidic stannous (Sn–II) solutions was found to be more effective and could be used for electrodeposition on circuit boards with patterned photoresist. The major disadvantage of these baths is their complicated compositions (which are difficult to control) since various additives, such as cresol and/or methane sulphonic acid, gelatine, cresylic acid, etc., had to be added in order to improve deposit morphology and adhesion. Recently, slightly acidic ammonium citrate – SnCl_2 electrolyte was used for pulsed electrodeposition of tin and optimum conditions for obtaining compact and flat deposit were defined.²⁰

The process of Sn electrodeposition from the pyrophosphate solution onto copper electrode has been investigated by Neveu et al.²¹ Based on the previous papers^{22,23} the authors proposed following deposition mechanism:



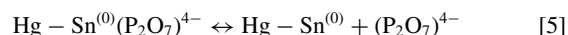
Concerning the mechanism proposed by the reactions 1 and 2 it should be stated that in Ref. 23–26 the mechanism is explained in a slightly different way and is valid for the polarographic investigation of Sn electrodeposition at the concentration of Sn^{2+} ions of 1×10^{-4} M:



(M^+ corresponds to the cation of supporting electrolyte) followed by the slow electrochemical step;



and the reversible chemical step;



assuming that $[\text{Sn}(\text{P}_2\text{O}_7)]^{2-}$ species are adsorbed in the outer Helmholtz plane of the double layer.

Considering all that has been mentioned above, it appears that more detailed analysis of the electrodeposition of Sn and Ni from the electrolytes containing only pyrophosphate and/or glycine was needed in order to better understand the process of Ni–Sn alloys electrodeposition. The results of such analysis are presented in this work.

^z E-mail: vladajovic@imsi.rs

Experimental

The experiments on the stationary glassy carbon (GC, surface area 0.636 cm²), Ni (surface area 0.196 cm²) and 40 nm thick Cu layer evaporated onto Si(111) electrodes (surface area 1.0 cm²) were carried out in a standard electrochemical cell with Pt counter electrode (placed in parallel with the working electrode) and saturated calomel electrode (SCE) as the reference electrode, both placed in a separate compartments. In all cases experiments were performed at the temperature of 25 ± 1 °C using potentiostat Reference 600 and software PHE 200 (Gamry Instruments Inc.). All chemicals were p.a. quality dissolved in extra pure UV water (Smart2PureUV, TKA). In the case of Sn deposition onto 40 nm thick Cu layer evaporated onto Si(111) electrode commercial solution for Sn deposition (without additives for brightness and leveling) containing 0.5 M Sn-MSA + 1.0 M MSA (MSA – methane sulfonic acid) was used and Sn wire immersed in the same solution was used as the reference electrode.

Before each experiment GC and Ni disk electrodes were mechanically polished down to 0.05 μm with alumina suspension, kept in the ultrasonic bath for 10 min and washed with UV water. In the case of Ni disk electrode, subsequent etching in a mixture HNO₃/H₂O = 3/1 for 10 s was performed in order to remove oxide layer from Ni surface. Electrode surface of 40 nm thick Cu layer evaporated onto Si(111) was cleaned in 0.1 M H₂SO₄ for 60 s before the deposition of Sn.

The appearance and the composition of deposits were investigated by SEM, Tescan, VEGA TS 5130 MM equipped with an energy-dispersive X-ray spectroscopy (EDS), INCA PentaFET-x3, Oxford Instruments.

The distribution of Ni and Sn complexes in the investigated solutions was obtained with the commercial software HySS2009 (Protonic Software).

Results and Discussion

Distribution of Ni and Sn complexes in the investigated solutions.— In the data presented in Dean's Handbook of Chemistry²⁷ Ni forms two pyrophosphate complexes, [Ni(Pyrr)₂]²⁻ and [Ni(Pyrr)₂]⁶⁻ and three glycine complexes, [Ni(Gly)]⁺, [Ni(Gly)₂]⁺ and [Ni(Gly)₃]⁻. There are only three papers in the literature with the data for different complexes of Ni and Sn in the pyrophosphate and glycine solutions. The data proposed by Duffield et al.,²⁸ Turyan et al.²⁹ and Orekhova et al.,³⁰ with corresponding reactions for different complexes formation and their formation (stability) constants are given in the work of Duffield et al.²⁸ In the paper of Djurdjevic et al.³¹ three complexes of Sn with glycine were detected, [SnH(Gly)]²⁺, [Sn(Gly)]⁺ and [Sn(Gly)OH]. These complexes exist at pH < 4, with the complex [Sn(Gly)OH] dominating at pH 4, while the same complex was found to precipitate at pH > 5. Since the pH of the solution for Ni–Sn alloy coatings electrodeposition amounts to 8.0, these data were not relevant for our work. Considering all the data available in the literature^{27–31} we decided to analyze system given in the paper of Turyan et al.²⁹ All species and their stability constants used for the calculation of the distribution of different complexes in the solution containing Sn, Ni, pyrophosphate and glycine ions are listed in Table I. According to the calculation of the distribution of complexes in the solution containing pyrophosphate and glycine, dominant complex with Sn at pH 8.0 is [Sn(Pyrr)₂]⁶⁻ (93.4%), while two complexes of Ni dominate: complex [Ni(Pyrr)₂]⁶⁻ (37.7%), and complex [Ni(Gly)₃]⁻ (47.0%). The values of the equilibrium potentials of prevailing complexes, calculated using explanations based on the Gibbs energy change for reaction of certain complex formation³² (assuming that the ions activity is equal to their concentrations), are also presented in Table I. As can be seen, the equilibrium potential for deposition of Sn by the reduction of [Sn(Pyrr)₂]⁶⁻ complex amounts to -0.845 V, while the equilibrium potentials for the reduction of [Ni(Pyrr)₂]⁶⁻ and [Ni(Gly)₃]⁻ complexes are more positive, being about -0.728 V. Hence, it could be concluded that at pH 8.0 Sn would deposit from the complex [Sn(Pyrr)₂]⁶⁻,

Table I. All complexes present in the solution 0.1 M SnCl₂ + 0.1 M NiCl₂ + 0.6 M K₄(Pyr) + 0.3 M Gly, their stability constants and equilibrium potentials of prevailing complexes.

Complexes	log β	Conc. /%	E _{eq} / V vs. SCE
[H(Pyrr)] ³⁻	8.14		
[H ₂ (Pyrr)] ²⁻	14.01		
[H ₃ (Pyrr)] ⁻	15.78		
[H ₄ (Pyrr)]	16.63		
[H(Gly)]	9.64		
[H ₂ (Gly)] ⁺	12.05		
[Sn(Gly)H] ²⁺	12.78		
[Sn(Gly)] ⁺	10.02		
[Sn(Pyrr)] ²⁻	13.05	6.6	
[Sn(Pyrr)H] ⁻	15.92		
[Sn(Pyrr)H ₂]	17.47		
[Sn(Pyrr) ₂] ⁶⁻	16.27	93.4	-0.845
[Sn(Pyrr) ₂ H] ⁵⁻	22.31		
[Sn(Pyrr) ₂ H ₂] ⁴⁻	26.79		
[Sn(Pyrr) ₂ H ₃] ³⁻	30.07		
[Sn(Pyrr) ₂ H ₄] ²⁻	31.58		
[Sn(Pyrr)OH] ³⁻	5.32	6.6	
[Sn(Pyrr)(OH) ₂] ²⁻	-4.77		
[Sn(Pyrr) ₂ OH] ⁵⁻	7.04		
[Ni(Gly)] ⁺	5.60		
[Ni(Gly) ₂]	10.40	8.7	
[Ni(Gly) ₃] ⁻	13.80	47.0	-0.728
[Ni(Pyrr)] ²⁻	5.80		
[Ni(Pyrr) ₂] ⁶⁻	7.40	37.7	-0.728

while Ni would deposit simultaneously from [Ni(Pyrr)₂]⁶⁻ and [Ni(Gly)₃]⁻ complexes in the presence of both complexing anions.

Electrodeposition of Sn from pyrophosphate solution.— The process of Sn electrodeposition from the pyrophosphate solution (0.1 M SnCl₂ + 0.6 M K₄P₂O₇, pH 8.0) is investigated by CV, polarization measurements, potentiostatic pulse experiments and SEM-EDS analysis onto stationary Ni and GC disk electrodes.

The results presented in Fig. 1a represent only the first sweeps recorded on both electrodes at the sweep rate of 10 mV s⁻¹, since electrodeposited Sn could not be completely dissolved during the anodic cycle from both substrates (remained Sn deposit could be seen by naked eye), starting from the potential of -0.8 V. The peaks **1a** and **2a** correspond to the partial dissolution and subsequent oxidation of electrodeposited Sn and before each experiment remained layer of Sn and Sn-oxide had to be removed from the electrode surface by polishing procedure. Considering results presented in Fig. 1a, it appears that the deposition of Sn at a given sweep rate commences at about -0.9 V (peak **1c**) onto Ni electrode, while for deposition onto GC electrode higher overvoltage is needed and accordingly the deposition commences at about -0.99 V (peak **1c**). The reversible potential of Sn deposition (point ●, where reverse sweeps on both substrates cross the zero current line) is positioned at -0.90 V for both substrates.

The polarization curves, obtained with the sweep rate of 1 mV s⁻¹, presented in Fig. 1b are in accordance with the CV's. The deposition of Sn onto Ni electrode is characterized with a sharp increase of cathodic current density at -0.90 V and a peak between -0.90 V and -1.00 V, followed with the increase of cathodic current density at potentials more negative than -1.10 V. The increase of cathodic current density at about -0.90 V for GC electrode indicates the beginning of Sn deposition onto GC electrode (dotted line) reaching the diffusion limiting current density at more negative potentials. Much sharper increase of the current density and a peak on the polarization curve for Sn deposition onto Ni indicates faster nucleation of Sn at the Ni surface in comparison with that on the GC surface. The same results as those presented in Figs. 1 and 2 are obtained in the

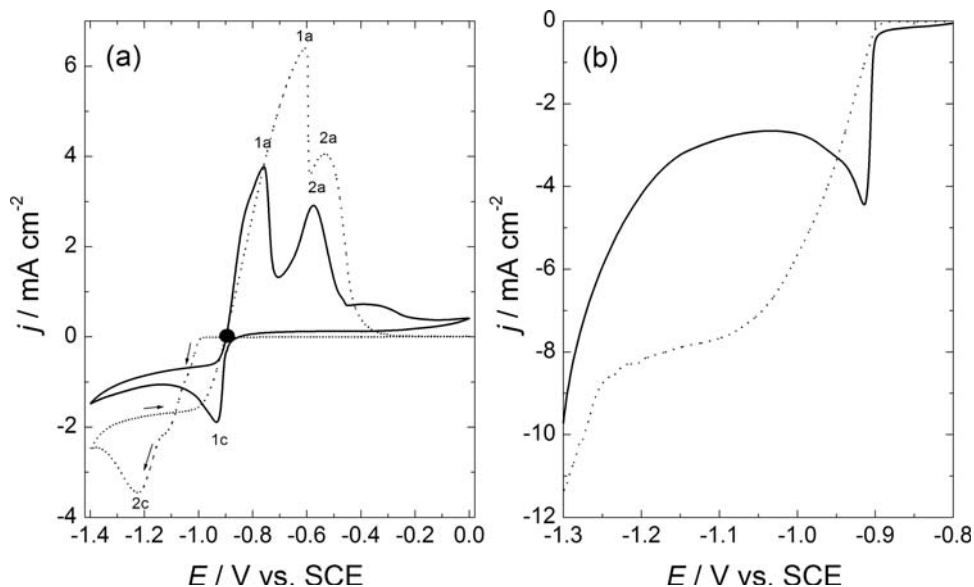


Figure 1. (a) Cyclic voltammograms (only the first sweeps) recorded onto stationary Ni (solid line) and GC (dotted line) disk electrodes at the sweep rate of 10 mV s^{-1} in the solution $0.1 \text{ M SnCl}_2 + 0.6 \text{ M K}_4\text{P}_2\text{O}_7$ of the pH 8.0 (starting potential $E = -0.80 \text{ V}$). (b) Polarization curves recorded onto stationary Ni (solid line) and GC (dotted line) disk electrodes at the sweep rate of 1 mV s^{-1} in the solution $0.1 \text{ M SnCl}_2 + 0.6 \text{ M K}_4\text{P}_2\text{O}_7$ of the pH 8.0 (starting potential $E = -0.80 \text{ V}$).

solution containing $0.1 \text{ M SnCl}_2 + 0.6 \text{ M K}_4\text{P}_2\text{O}_7 + 0.3 \text{ M Glycine}$ of pH 8.0.

The potentiostatic pulse $j-t$ transients for Sn deposition onto GC electrode, recorded at different potentials between -0.90 V and -1.15 V , are presented in Fig. 2. The shape of these transients (Fig. 2a) is characteristic for 3D nucleation and growth.^{33–37} According to the theory of 3D nucleation and growth by the analysis of the

rising portion of $j-t$ transients, before the beginning of the overlapping of 3D nuclei, it is possible to determine the type of nucleation (instantaneous or progressive).^{33–37} As can be seen for $j-t$ transients recorded at potentials -0.99 V and -1.01 V only rising portions of the transients were recorded for 200 s, indicating formation of 3D crystals and their growth without overlapping between them. At more negative potentials of -1.05 V and -1.15 V the $j-t$ transients are characterized

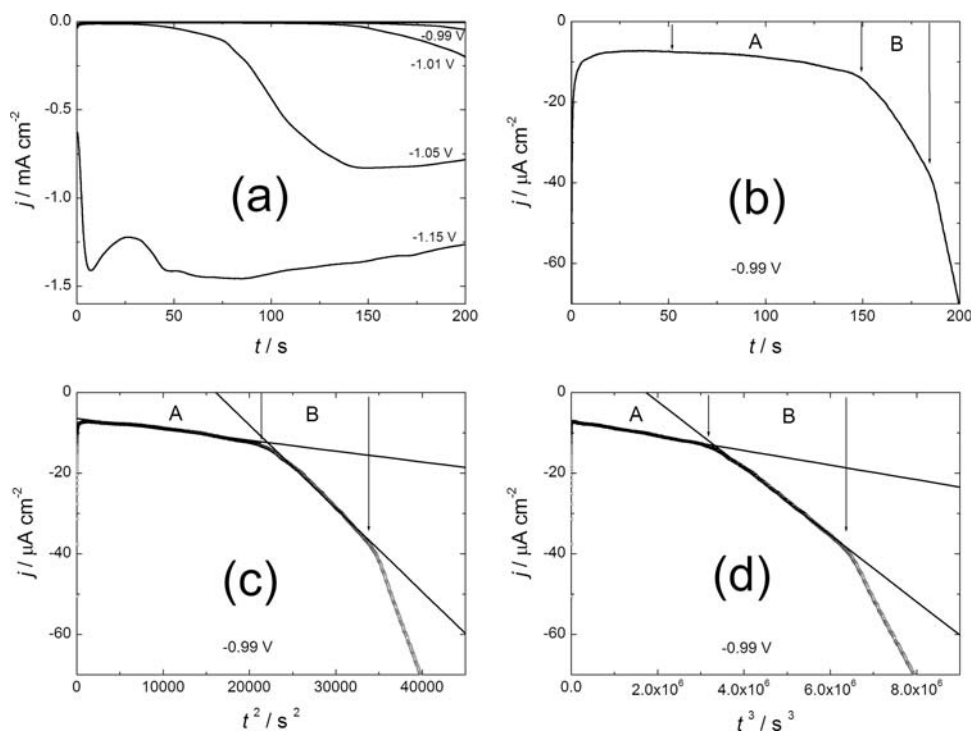


Figure 2. (a) Potentiostatic $j-t$ transients for Sn nucleation and growth onto GC electrode recorded at different potentials (marked in the figure); (b) Rising portion of the potentiostatic $j-t$ transient for the potential of -0.99 V ; (c) j vs. t^2 dependence for the response presented in (b); (d) j vs. t^3 dependence for the response presented in (b).

with the maximum current density and the decrease of current density after the maximum, indicating possible overlapping of the 3D crystals, or their diffusion zones.^{33–37} By theoretical consideration of different growth rates, shapes of growing crystallites, rate-determining steps and types of nucleation (instantaneous or progressive) j vs. t dependences corresponding to different 3D nucleation and growth mechanisms were developed in the literature and summarized in Table II. Taking into account the shape of the polarization curve for Sn deposition onto GC electrode it could be concluded that this process is controlled by charge transfer at potentials between -0.90 V and -1.15 V. Hence, assuming that 3D crystals possess either cone or hemispherical shape, their j vs. t^2 (instantaneous nucleation) or j vs. t^3 (progressive nucleation) dependences (see Table II) should be linear for the j - t transient recorded at the potential of -0.99 V (Fig. 2b). These dependences are shown in Figs. 2c and 2d respectively. As can be seen linear dependences were obtained for both, instantaneous and progressive nucleation and growth in the two time regions A and B. Such behavior indicates that none of the proposed models could be applied to the 3D nucleation and growth of Sn. The appearance of the Sn deposit obtained for the j - t transient recorded at the potential of -1.05 V (Fig. 2a) is shown in Fig. 3a and 3b. The isolated 3D crystals of Sn possess rectangular shape (Fig. 3b) and each 3D crystal grows normally to the electrode surface without any overlapping between them (Fig. 3a and 3b). It seems that neither the shape nor the growth mode for Sn nucleation and growth fit any of the models predicted in the literature.^{33–37}

In order to investigate the nucleation and growth of Sn in the commercial bath for tin electrodeposition (without additives for brightness and leveling), experiments were performed in the solution containing 0.5 M Sn-MSA + 1.0 M MSA on the 40 nm thick Cu layer evaporated onto Si(111). Two overpotentials were chosen: -20 mV and -60 mV. Corresponding j - t transients are presented in Fig. 4a and 4d. Well defined rising portion of the transient recorded for -20 mV, Fig. 4a, was analyzed by plotting j vs. t^2 and j vs. t^3 dependences, as shown in Fig. 4b and 4c. As in the case of Sn 3D nucleation and growth from pyrophosphate solution onto GC electrode (Fig. 2c and 2d), linear dependences were obtained for both, instantaneous and progressive nucleation and growth in the two time regions, showing again that 3D nucleation and growth of Sn does not fit any of the predicted models. The j - t transient recorded for -60 mV is presented in Fig. 4d. Taking into account the shape of the j - t transient it seems that at a given overpotential hemispherical diffusion is rate-determining step and that theoretical approach developed by Hills et al.^{38,39} could be applied. Theoretical curves (non-dimensional dependences $(j/j_m)^2$ vs. (t/t_m)) for the instantaneous and progressive nucleation for such case are presented by solid and dotted lines respectively, while the analysis of the experimentally recorded j - t transient are presented by open circles (\circ). Again, certain discrepancy between the model and the experimental results is obvious. The appearances of the deposits obtained at -20 mV and -60 mV are presented in Fig. 5a and 5b respectively. Large rectangular Sn crystals, growing mainly perpendicular to the electrode surface are obtained for lower overpotential (Fig. 5a), while large number of smaller rectangular Sn crystals, growing perpendicular to the electrode surface are obtained for higher overpotential (Fig. 5b). Considering the shape of nuclei it seems that the discrepancy between theoretical and experimental curves in Fig. 4e is due to theoretical assumption that nuclei and their diffusion zones are hemispherical,^{38,39} while in the experiment the nuclei are rectangular and their diffusion zones should be different than hemispherical. Similar results were obtained for Sn 3D nucleation and growth onto Pt electrode from citrate containing solution.⁴⁰

The appearance of the Sn deposit onto Ni electrode, obtained by the potentiostatic pulse for 1000 s at -1.15 V, is presented in Fig. 6. As can be seen, thick, but not dense (compact) Sn deposit is formed all over the electrode surface, while on few places of the electrode surface deposit is much thinner and less dense (marked with A in Fig. 6a and presented in Fig. 6b at higher magnification). In Fig. 6c EDS analysis was performed at two positions of thick compact Sn deposit. At the top of a large (about 2 μm) Sn crystal (spectrum 1)

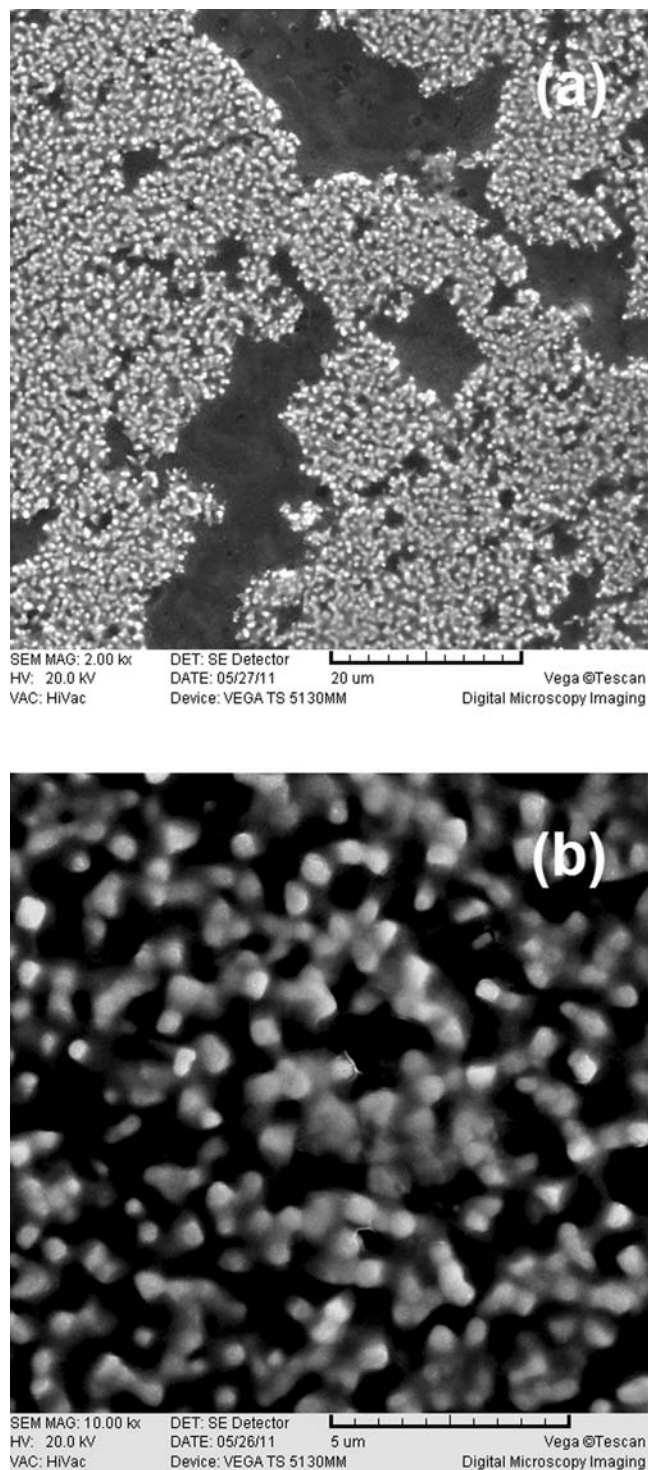


Figure 3. SEM micrographs of the Sn deposit obtained onto GC electrode during the potentiostatic pulse $E = -1.05$ V for 200 s in the solution 0.1 M SnCl_2 + 0.6 M $\text{K}_4\text{P}_2\text{O}_7$ of the pH 8.0 : part of the surface with more dense (a) and less dense (b) deposit.

94 atom% Sn and 6 atom% Ni were detected, while at the position of thinner Sn deposit (spectrum 2) the composition was 76 atom% Sn and 24 atom% Ni. It appears that at 20 kV the EDS beam penetrates deeper than the thickness of the deposit detecting more Ni from the substrate at the position of thinner deposit. Almost identical morphology of Sn deposit onto gold surface has been obtained from ammonium citrate solution.³² Hence, it could be concluded that

Table II. The j vs. t dependences for different nucleation types, growth modes, and rate-determining steps (Ref. 33).^a

Growth mode	Shape of growing crystallites	Rate-determining step	Nucleation type	j vs. t	
1D	needles	charge transfer	instantaneous	$j = K_0$	
			progressive	$j = K_1 t$	
2D	disks	charge transfer	instantaneous	$j = K_2 t$	
			progressive	$j = K_3 t^2$	
		cylindrical diffusion	instantaneous	$j = K_4$	
			progressive	$j = K_5 t$	
3D	cones	charge transfer	instantaneous	$j = K_6 t^2$	
			progressive	$j = K_7 t^3$	
		hemispheres	charge transfer	instantaneous	$j = K_8 t^2$
				progressive	$j = K_9 t^3$
	hemispherical diffusion	instantaneous	instantaneous	$j = K_{10} t^{1/2}$	
			progressive	$j = K_{11} t^{3/2}$	
		ohmic control	instantaneous	instantaneous	$j = K_{12} t^{1/2}$
				progressive	$j = K_{13} t^{3/2}$

^a Constants $K_0 - K_{13}$ are composed of different parameters defining crystal growth, such as: radius of the growing nuclei; rate of normal and lateral growth of nuclei; height of growing disks; growth rate by hemispherical growth; mutual diffusion coefficient of Me^{z+} ; electrolyte conductivity; etc.

under the conditions of constant potential (overpotential) it is practically not possible to obtain compact and flat Sn deposit from the investigated solutions (without additives for brightening and leveling) independently of the materials and type of the electrode surface. At the same time the growth type and the shape of 3D Sn crystals do not fit any of the predicted models in the literature.^{33–37} It seems that after initial formation of rectangular 3D Sn crystals further growth of existing crystals occurs only normally to the electrode surface, indicating that none of the models predicted in the literature could be operative.

Electrodeposition of Ni.— Polarization curves recorded at the Ni disk electrode with the sweep rate of 1 mV s^{-1} in the solution of 0.1 M $\text{NiCl}_2 + 0.3 \text{ M Glycine}$ at pH 8.0 (curve 1), 0.1 M $\text{NiCl}_2 + 0.3 \text{ M Glycine}$ at pH 3.8 (curve 2) and 0.1 M $\text{NiCl}_2 + 0.6 \text{ M K}_4\text{P}_2\text{O}_7$ at pH 8.0 (curve 3) are presented in Fig. 7 (starting potential was set at -0.70 V). Significant difference in the shape of the polarization curves for Ni deposition in pure glycine solution at different pH values is observed, while the potentials of the beginning of the deposition process differ for about 0.21 V (marked with arrows). Similar shape of the polarization curves for Ni deposition in pure pyrophosphate

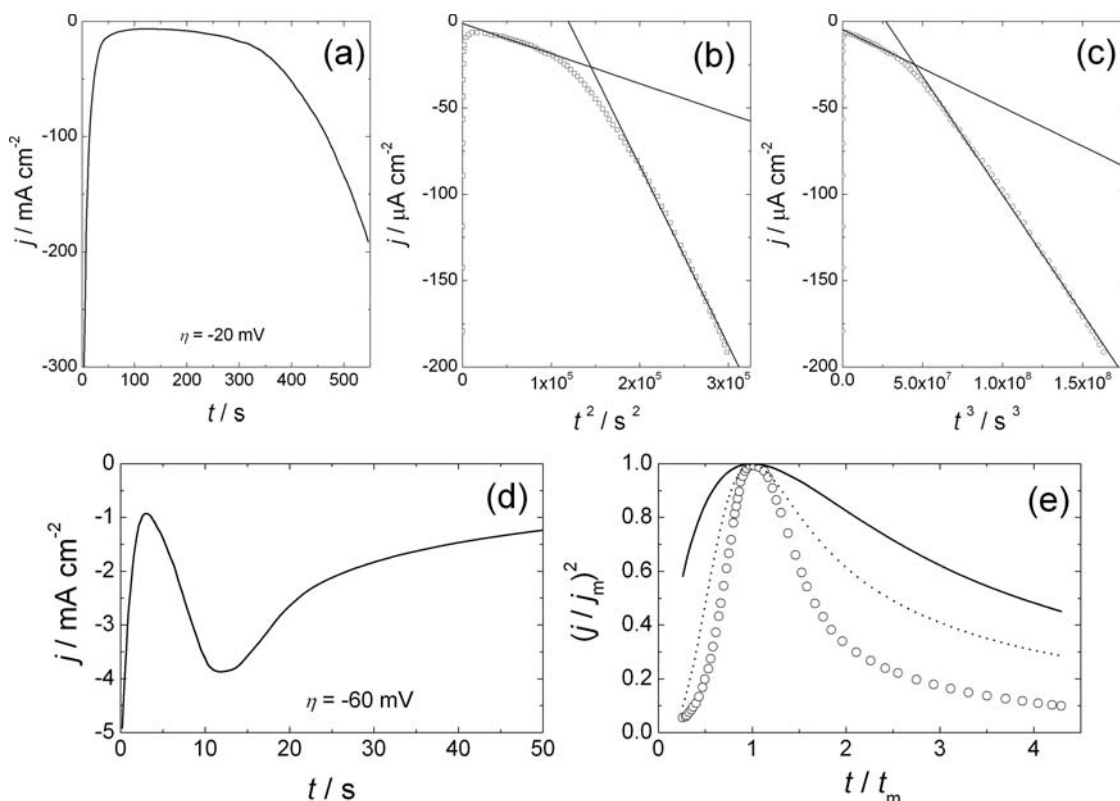


Figure 4. (a) Rising portion of the potentiostatic j - t transient recorded for the overpotential of -20 mV on the 40 nm thick Cu layer evaporated onto Si(111) in the solution containing 0.5 M Sn-MSA + 1.0 M MSA; (b) j vs. t^2 dependence for the response presented in (a); (c) j vs. t^3 dependence for the response presented in (a); (d) the potentiostatic j - t transient recorded for the overpotential of -60 mV ; (e) $(j/j_m)^2$ vs. (t/t_m) dependence for the transient presented in (d) – theoretical dependence for instantaneous nucleation (solid line), theoretical dependence for progressive nucleation (dotted line), experimental points (\circ).

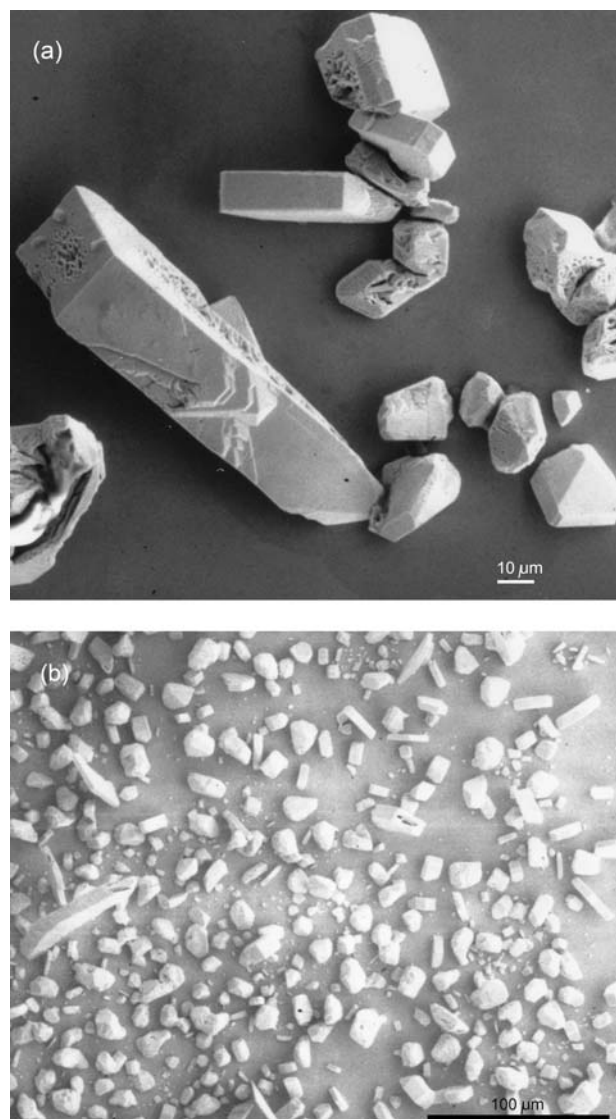


Figure 5. SEM micrographs of the Sn deposit obtained on the 40 nm thick Cu layer evaporated onto Si(111) in the solution containing 0.5 M Sn-MSA + 1.0 M MSA obtained at the overpotential of -20 mV (a) and -60 mV (b).

(curve 3) and pure glycine solutions (curve 1) at the pH 8.0 indicates that the process of Ni deposition from pyrophosphate and/or glycine complexes is similar, with the Ni deposition starting at about -0.96 V in both solutions. As can be seen, Ni deposition starts at the most positive potential in pure glycine solution of the pH 3.8 (curve 2). The reversible potential for Ni deposition from the Ni^{2+} ions (prevailing in this solution, see inset of Fig. 7) amounts to about -0.48 V. According to the slow increase of current density at potentials between -0.73 V and -0.87 V we believe that Ni deposition (forming epitaxial Ni layer typical for Ni deposition) takes place in this potential region since certain overvoltage for Ni deposition should be applied⁴¹ and that at more negative potentials this process is accompanied with simultaneous hydrogen evolution, taking into account that the reversible potential for HER at the pH 3.8 amount to -0.48 V and that for this reaction certain overvoltage is also needed. In the presence of pyrophosphate (curve 3), potential of the beginning of Ni deposition and hydrogen evolution is moved to more cathodic values, indicating higher overvoltage for Ni deposition in the presence of pyrophosphate, as well as more negative potential for hydrogen evolution since the pH of this solution amounts to 8.0 (curves 1 and 3). Such behavior is most likely due to Ni deposition from different complexes: in the solution of the pH 8.0 complexes $[\text{Ni}(\text{Gly})_2]$ and $[\text{Ni}(\text{Gly})_3]^-$ prevail, while in the solution

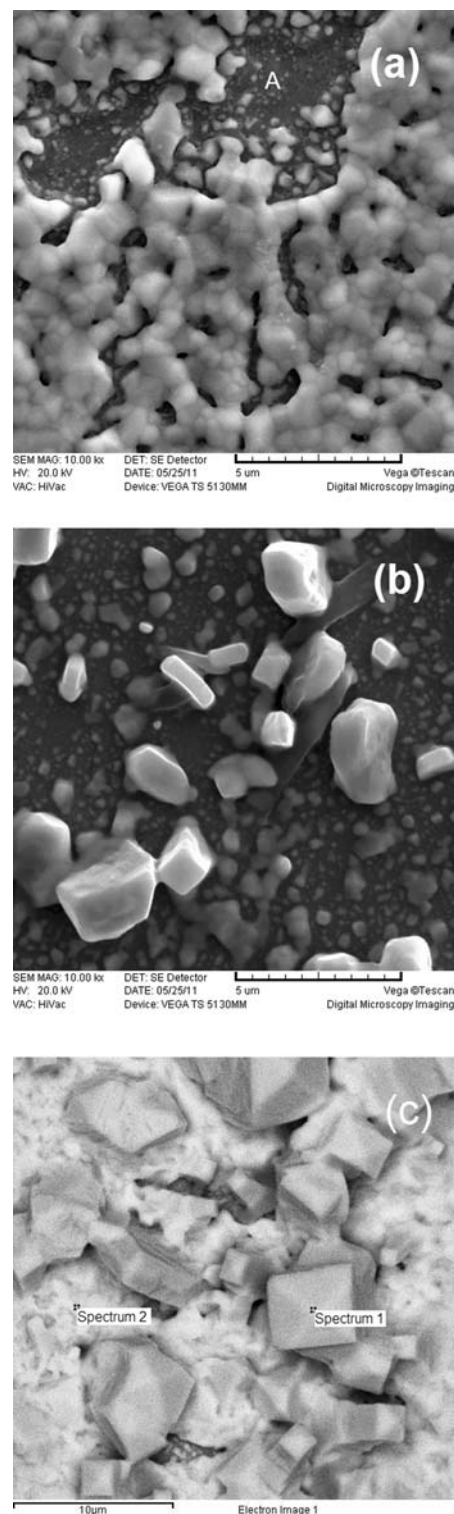


Figure 6. SEM micrographs of the Sn deposit obtained onto Ni electrode during the potentiostatic pulse $E = -1.15$ V for 1000 s in the solution 0.1 M $\text{SnCl}_2 + 0.6$ M $\text{K}_4\text{P}_2\text{O}_7$ of the pH 8.0: (a) part of the surface with more dense and less dense (A) deposit; (b) position marked with A in (a) recorded at higher magnification; (c) SEM-EDS of compact deposit (spectrum 1–94 atom% Sn and 6 atom% Ni, spectrum 2–76 atom% Sn and 24 atom% Ni).

of the pH 3.8 hydrated Ni^{2+} ions prevail (75%) and the rest of nickel is present as $[\text{Ni}(\text{Gly})]^+$ complex (25%) (see inset of Fig. 7).

According to the data presented in Table I, reversible potential for Ni deposition from either pyrophosphate or glycine complex amounts

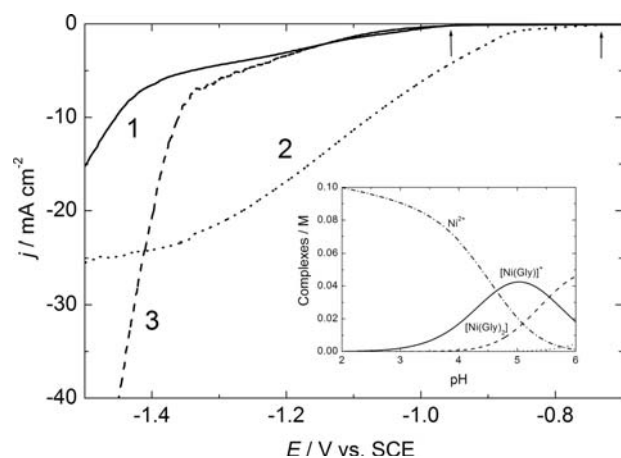


Figure 7. Polarization curves recorded onto Ni disk electrode with the sweep rate of 1 mV s^{-1} in the solution $0.1 \text{ M NiCl}_2 + 0.3 \text{ M Glycine}$ of the pH 8.0 (curve 1), $0.1 \text{ M NiCl}_2 + 0.3 \text{ M Glycine}$ of the pH 3.8 (curve 2) and $0.1 \text{ M NiCl}_2 + 0.6 \text{ M K}_4\text{P}_2\text{O}_7$ of the pH 8.0 (curve 3): inset – distribution of Ni complexes in pure glycine (0.3 M Glycine) solution as a function of pH from 2 to 6.

to -0.728 V , while the deposition is seen to start at more negative potential (-0.96 V), which is not surprising taking into account that certain overpotential for Ni deposition is needed.⁴¹

Electrodeposition of Ni–Sn alloy from the solution containing pyrophosphate and glycine anions.— The polarization curves recorded onto GC and Ni disk electrodes with the sweep rate of 1 mV s^{-1} in the solution of $0.1 \text{ M SnCl}_2 + 0.1 \text{ M NiCl}_2 + 0.6 \text{ M K}_4\text{P}_2\text{O}_7 + 0.3 \text{ M Glycine}$ of pH 8.0, are presented in Fig. 8. According to the results presented in Fig. 7, Ni deposition commences at about -0.96 V and the Ni–Sn alloy formation could be expected at potentials more negative than -0.96 V onto GC electrode, since the deposition of Sn onto GC electrode commences at the potential of -0.90 V (Fig. 1b). In the case of Ni electrode (Fig. 8) deposition of Ni–Sn alloy commences at slightly more positive potential of about -0.86 V . The current density plateaus for both electrodes indicate diffusion limiting process of Ni–Sn alloy deposition in the potential range from about -1.05 V to about -1.20 V , while at more negative potentials simultaneous hydrogen evolution occurs. It is interesting to note that the diffusion limiting current density for Ni–Sn alloy deposition onto GC electrode is about two times lower than that onto Ni electrode. This could be the consequence of much rougher Ni surface due to formation of

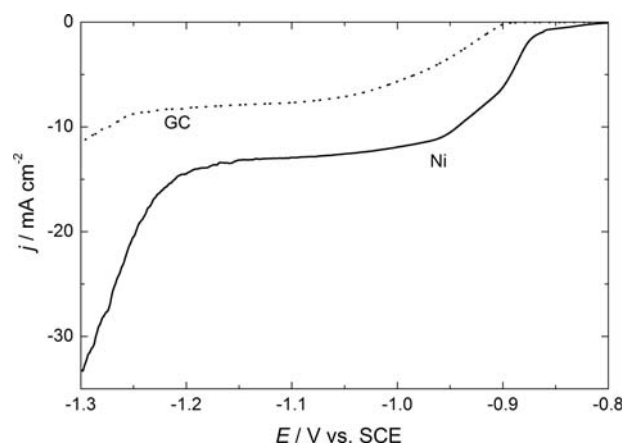


Figure 8. Polarization curves recorded onto GC and Ni electrodes (marked in the figure) with the sweep rate of 1 mV s^{-1} in the solution $0.1 \text{ M SnCl}_2 + 0.1 \text{ M NiCl}_2 + 0.6 \text{ M K}_4\text{P}_2\text{O}_7 + 0.3 \text{ M Glycine}$ of the pH 8.0.

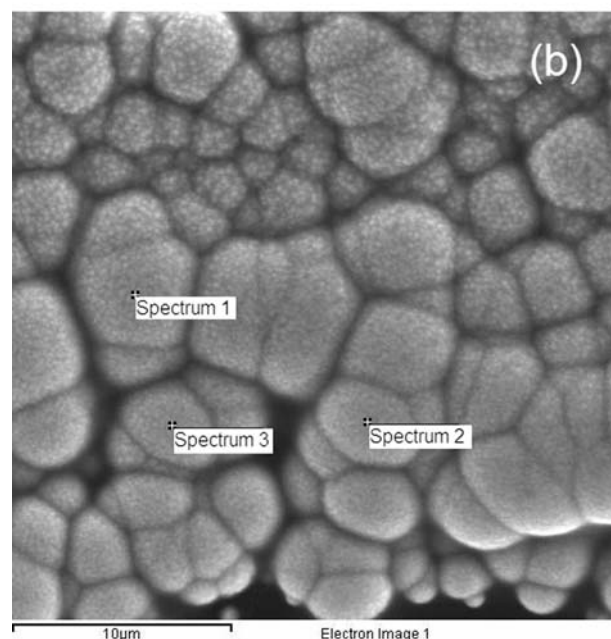
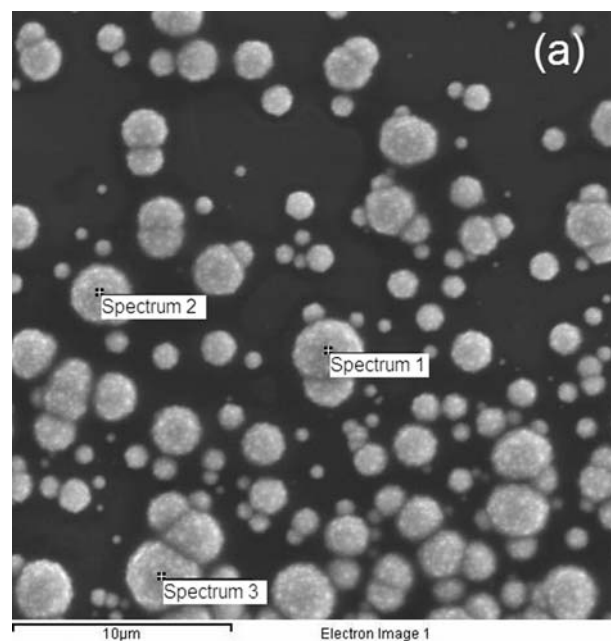


Figure 9. SEM micrographs with the positions of EDS analysis of the Ni–Sn deposit obtained onto GC electrode during the potentiostatic pulse $E = -1.00 \text{ V}$ for 1000 s in the solution $0.1 \text{ M SnCl}_2 + 0.1 \text{ M NiCl}_2 + 0.6 \text{ M K}_4\text{P}_2\text{O}_7 + 0.3 \text{ M Glycine}$ of the pH 8.0: (a) less dense deposit, average composition 54 atom% Ni – 46 atom% Sn; (b) dense deposit, average composition 47 atom% Ni – 53 atom% Sn.

bigger Sn crystals in comparison with those onto GC electrode (Figs. 3 and 6). At the same time, by comparing results presented in Fig. 1b and Fig. 8 it could be concluded that the diffusion limiting current densities for Ni–Sn alloy deposition are approximately two times higher than those for pure Sn deposition onto GC electrode ($j_{l(\text{Sn})} \approx -4 \text{ mA cm}^{-2}$, $j_{l(\text{Ni-Sn})} \approx -8 \text{ mA cm}^{-2}$), indicating that the composition of the Ni–Sn alloy deposit in the range of the diffusion limiting current densities should be about 50 atom% Ni – 50 atom% Sn. One sample of the Ni–Sn alloy was deposited potentiostatically for 1000 s at the potential of -1.00 V onto GC electrode and its morphology and composition were investigated by SEM and EDS. The results are presented in Fig. 9. With the total cathodic charge of approximately

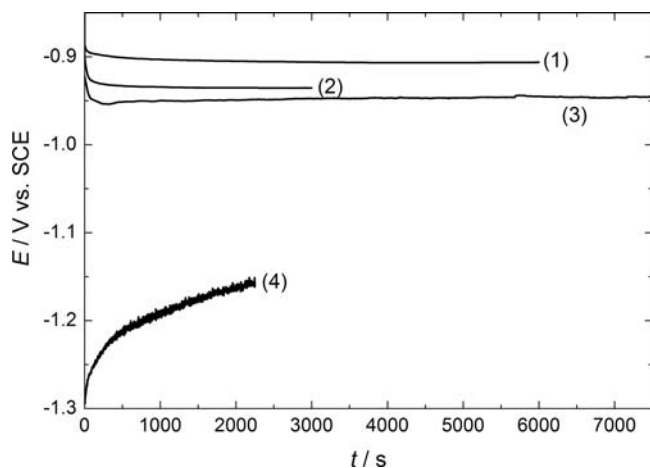


Figure 10. Potential vs. time (E vs. t) responses for deposition of Ni-Sn alloy coatings at different current densities: (1) $j = -2.5 \text{ mA cm}^{-2}$, $t = 6000 \text{ s}$; (2) $j = -5.0 \text{ mA cm}^{-2}$, $t = 3000 \text{ s}$; (3) $j = -6.0 \text{ mA cm}^{-2}$, $t = 7500 \text{ s}$; (4) $j = -20.0 \text{ mA cm}^{-2}$, $t = 2250 \text{ s}$.

6 C cm^{-2} such deposit should be thick and compact. Considering the morphology of the deposit, presented in Fig. 9a and 9b, it is obvious that this is not the case. The whole surface of the GC electrode is not covered with the deposit and two regions could be detected: region with the isolated 3D crystals (Fig. 9a) and region with a compact deposit (Fig. 9b). As can be seen in Fig. 9a all crystals possess ball-like shape in the region where overlapping didn't take place, while in the compact deposit (Fig. 9b) overlapping of 3D crystals caused distortion of ball-like crystals. The EDS analysis of ball-like crystals (Fig. 9a) gave an average composition of 54 atom% Ni – 46 atom% Sn, while average composition of compact deposit (Fig. 9b) was found to be 47 atom% Ni – 53 atom% Sn. It should be emphasized here that two deposited metals, Ni and Sn, are characterized by two different growth mechanisms: Ni is known to form compact deposit with characteristic of epitaxial growth, while Sn forms isolated 3D crystals and compact deposits could be obtained only in the presence of strong additives. It seems that the morphology dictated by Sn 3D nucleation and growth prevails in the Ni-Sn alloy deposit obtained onto GC electrode, since about 20% of the deposit is in the form presented in Fig. 9a.

By comparing results presented in Figs. 3 and 9 it could be concluded that the shape of crystals of pure Sn and Ni-Sn alloy are different. The Ni-Sn alloy crystallizes in the shape of ball-like crystals, while pure Sn crystals are characterized by the rectangular shape.

To determine the current efficiency (η_j) and the influence of the current density on the composition of the Ni-Sn alloy, four samples

Table III. Composition and current efficiencies for Ni-Sn alloy samples electrodeposited at different current densities.

Sample no.	$-j / \text{mA cm}^{-2}$	Spectrum no.	atom% Ni	atom% Sn	$\eta_j / \%$
(1)	2.5	1	32	68	88
		2	33	67	
(2)	5.0	1	40	60	84
		2	40	60	
		3	40	60	
(3)	6.0	1	45	55	80
		2	45	55	
		3	46	54	
(4)	20	1	50	50	70
		2	47	53	
		3	42	58	

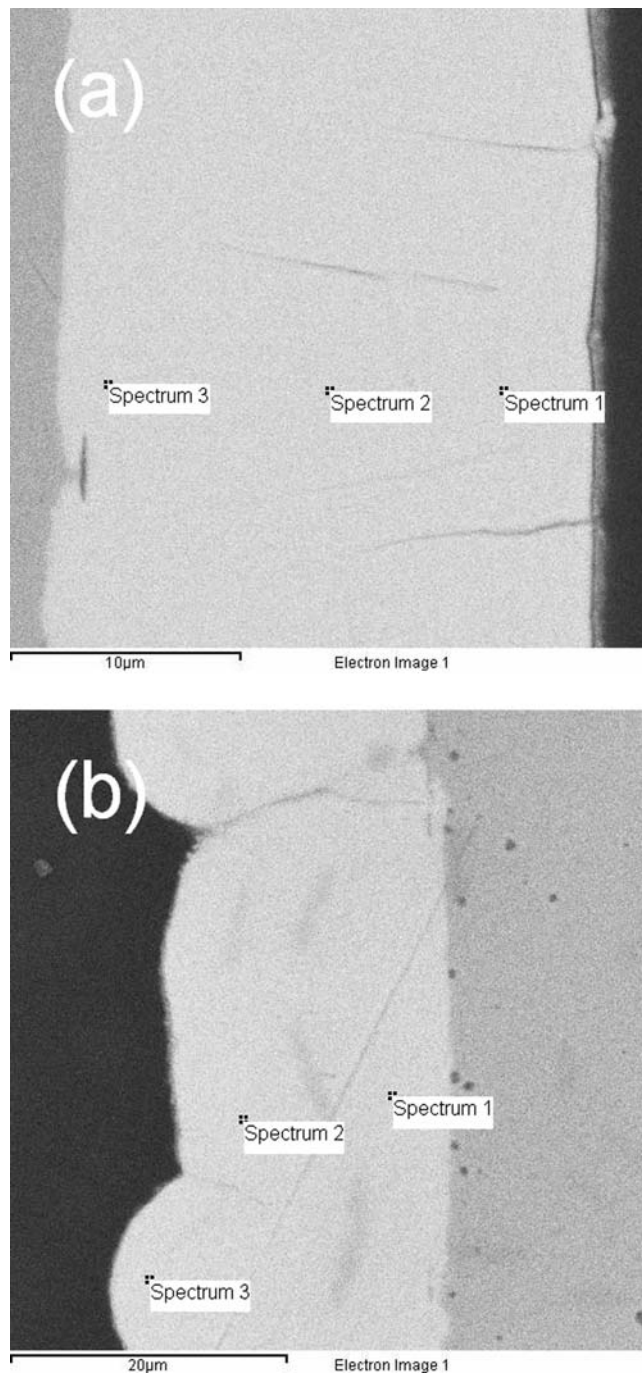


Figure 11. (a) SEM-EDS of a cross-section of sample (3), (b) SEM-EDS of a cross-section of sample (4).

were deposited onto Ni disk electrode at different current densities and deposition times: (1) $j = -2.5 \text{ mA cm}^{-2}$, $t = 6000 \text{ s}$; (2) $j = -5.0 \text{ mA cm}^{-2}$, $t = 3000 \text{ s}$; (3) $j = -6.0 \text{ mA cm}^{-2}$, $t = 7500 \text{ s}$; (4) $j = -20.0 \text{ mA cm}^{-2}$, $t = 2250 \text{ s}$. Corresponding potential vs. time responses for deposition for all samples are presented in Fig. 10. The current efficiencies, measured as the difference between the sample mass after and before deposition, are given in Table III together with the composition of the Ni-Sn alloy samples obtained by the EDS analysis of their cross-sections. The cross-sections of samples (3) and (4) are presented in Fig. 11a and 11b respectively. As can be seen in Fig. 11 flat and compact deposit was obtained for sample (3), as well as for samples (1) and (2) (not shown in this work), which were

deposited with the current densities lower than the diffusion limiting one ($j_d \approx 12.0 \text{ mA cm}^{-2}$, Fig. 8) onto Ni electrode. At the highest current density of -20 mA cm^{-2} (which is not much higher than the diffusion limiting one) the deposit is rough, as shown in Fig. 11b. Accordingly, the current efficiencies for samples (1), (2) and (3) are higher than that for sample (4) (Table III). As shown in Table III the composition of samples (1)–(3) is uniform all over the cross-section (very similar composition is detected at all spectra positions), while for sample (4) the composition changes with the deposit thickness. The amount of Ni close to the substrate surface is higher than that at the surface of the deposit and consequently the amount of Sn increases over the cross-section (Fig. 11b) of sample (4). Taking into account that simultaneous hydrogen evolution occurs during the deposition of sample (4) it is possible that either intensive convection or local increase of the pH in the vicinity of the electrode surface produce the change of the Ni–Sn alloy composition over the cross-section of the deposit.

Since the Ni–Sn alloy coatings could be good catalyst for hydrogen evolution,^{13,14} our further research will be focused on the influence of chemical composition, phase composition and morphology of electrodeposited Ni–Sn alloy coatings on the hydrogen evolution reaction.

Conclusions

From the results of Sn electrodeposition in the pyrophosphate solution recorded at different substrates (Ni, GC), it could be concluded that the process of Sn electrodeposition on both electrodes commences at -0.90 V . Deposit is characterized by the presence of isolated 3D rectangular crystals growing perpendicular to the electrode surface with no overlapping between them onto GC substrate. The deposit obtained at the Ni electrode is denser on most of the surface, but at the certain part of the surface isolated 3D rectangular crystals could be detected. It is shown that 3D nucleation and growth of Sn onto GC electrode does not fit any theoretically predicted model. In the presence of Ni ions in the pyrophosphate/glycine solution the Ni–Sn alloy deposition commences at about -0.96 V onto Ni electrode producing thick and compact Ni–Sn alloy coating of different composition depending on the applied current density/potential. The Ni–Sn alloy deposit obtained onto GC electrode is characterized by the presence of isolated 3D crystals with no overlapping between them at the certain part of the electrode surface and denser deposit with overlapping between 3D crystals on the rest of the surface, with the ball-like shape of the Ni–Sn alloy crystals.

Acknowledgments

The authors are indebted to the Ministry of Education and Science of the Republic of Serbia (Project No. 172054) for the financial support of this work.

References

1. S. C. Britton and R. M. Angels, *J. Electrodep. Tech. Soc.*, **27**, 293 (1951).
2. S. A. M. Rafea, F. Taha, and T. H. A. Hasanin, *Electrochim. Acta*, **51**, 2942 (2006).
3. G. C. Wilson, *Trans. Inst. Met. Finish.*, **50**, 109 (1972).
4. S. K. Jalota, *Metal Finish.*, **99**, 320 (2001).
5. H. Jimenez, L. Gil, M. H. Staia, and E. S. Puchi-Cabrera, *Surf. Coat. Technol.*, **202**, 2072 (2008).
6. H. P. Zhao, C. Y. Jiang, X. M. He, J. G. Ren, and C. R. Wan, *Electrochim. Acta*, **52**, 7820 (2007).
7. J. Hassoun, S. Penero, and B. Scrosati, *J. Power Sources*, **160**, 1336 (2006).
8. F. S. Ke, L. Huang, H. H. Jiang, H. B. Wei, F. Z. Yang, and S. G. Sun, *Electrochem. Comm.*, **9**, 228 (2007).
9. J. Hassoun, S. Penero, P. Simon, P. L. Taberna, and B. Scrosati, *Adv. Mater.*, **19**, 1632 (2007).
10. D. Zhang, C. Yang, J. Dai, J. Wen, L. Wang, and C. Chen, *Trans. Nonferrous Met. Soc. China*, **19**, 1489 (2009).
11. J. A. Augis and J. E. Bennet, *J. Electrochem. Soc.*, **125**, 330 (1978).
12. E. W. Brooman, *Metal Finish.*, **99**, 100 (2001).
13. M. B. F. Santos, E. Peres Da Silva, R. Andrade Jr., and J. A. F. Dias, *Electrochim. Acta*, **37**, 29 (1992).
14. H. Yamashita, T. Yamamura, and K. Yoshimoto, *J. Electrochem. Soc.*, **140**, 2238 (1993).
15. A. G. Gray, *Modern Electroplating*, p. 387, John Wiley & Sons, Inc., New York (1953).
16. J. W. Cuthbertson, in *Tin and Its Alloys*, E. S. Hedges, Editor, p. 99, Edward Arnold Ltd., London (1960).
17. F. A. Lowenheim, *Electroplating*, p. 307, McGraw-Hill Book Company, New York (1978).
18. J. I. Duffy, *Electroplating Technology-Recent Developments*, p. 92, Noyes Data Corporation, Park Ridge, New Jersey (1981).
19. J. W. Price, *Tin and Tin Alloy Plating*, p. 5, Electrochemical Publications Ltd., Ayr, Scotland (1983).
20. A. He, Q. Liu, and D. G. Ivey, *J. Mater. Sci. Mater. Electron.*, **19**, 553 (2008).
21. B. Neveu, F. Lallemand, G. Poupon, and Z. Mekhalif, *Appl. Surf. Sci.*, **252**, 3561 (2006).
22. N. M. Martyak and R. Seefeldt, *Electrochim. Acta*, **49**, 4303 (2004).
23. V. I. Kravtsov and V. V. Kondratiev, *Electrochim. Acta*, **36**, 421 (1991).
24. V. V. Kondratiev and V. I. Kravtsov, *Elektrokhimiya*, **18**, 1502 (1982).
25. V. V. Kondratiev and V. I. Kravtsov, *Elektrokhimiya*, **23**, 1118 (1987).
26. V. I. Kravtsov, V.-V. Kondratiev, and I. Ya. Tur'yan, *Elektrokhimiya*, **24**, 1157 (1988).
27. J. A. Daen, *Lange's Handbook of Chemistry*, 15th Edition, McGraw-Hill Inc., New York (1999).
28. J. R. Duffield, D. R. Williams, and I. Kron, *Polyhedron*, **10**, 377 (1991).
29. I. Ya. Turyan, V. I. Kravtsov, and V. V. Kondratiev, *Elektrokhimiya*, **22**, 1388;1618 (1986).
30. V. V. Orekhova, F. K. Andryuschenko, and N. D. Sakhnenko, *Elektrokhimiya*, **16**, 1304 (1980).
31. P. Djurdjevic and D. Djokic, *J. Inorg. Biochem.*, **62**, 17 (1996).
32. C. Han, Q. Liu, and D. G. Ivey, *Electrochim. Acta*, **53**, 8332 (2008).
33. E. Budevski, G. Staikov, and W. J. Lorenz, *Electrochemical Phase Formation and Growth*, in *Advances in Electrochemical Science and Engineering*, R. C. Alkire, H. Gerischer, D. M. Kolb, and C. W. Tobias, Editors, VCH, Weinheim, New York, Basel, Cambridge, Tokyo (1996).
34. M. Fleischmann and H. R. Thirsk, in *Advances in Electrochemistry and Electrochemical Engineering*, p. 123, P. Delahay, Editor, Wiley, New York (1963).
35. J. A. Harrison and H. R. Thirsk, in *Electroanalytical Chemistry*, p. 67, A. J. Bard, Editor, Marcel Dekker, New York (1971).
36. G. J. Hills, D. J. Schiffrin, and J. Thompson, *Electrochim. Acta*, **19**, 657 (1974).
37. D. Kashchiev and K. Milchev, *Thin Solid Films*, **28**, 189 (1975).
38. B. Scharifker and G. Hills, *Electrochim. Acta*, **28**, 879 (1983).
39. G. Hills, A. K. Pour, and B. Scharifker, *Electrochim. Acta*, **28**, 891 (1983).
40. C. Han, Q. Liu, and D. G. Ivey, *Electrochim. Acta*, **54**, 3419 (2009). ubaciti
41. V. D. Jović and N. Tošić, *J. Electroanal. Chem.*, **441**, 69 (1998).